



Nano-plasmonics and electronics co-integration in CMOS enabling a pill-sized multiplexed fluorescence microarray system

LINGYU HONG,¹ HAO LI,² HAW YANG,² AND KAUSHIK SENGUPTA^{1,*}

¹Department of Electrical Engineering, Princeton University, NJ 08544, USA

²Department of Chemistry, Princeton University, NJ 08544, USA

*kaushiks@princeton.edu

Abstract: The ultra-miniaturization of massively multiplexed fluorescence-based bio-molecular sensing systems for proteins and nucleic acids into a chip-scale form, small enough to fit inside a pill ($\sim 0.1\text{cm}^3$), can revolutionize sensing modalities in-vitro and in-vivo. Prior miniaturization techniques have been limited to focusing on traditional optical components (multiple filter sets, lenses, photo-detectors, etc.) arranged in new packaging systems. Here, we report a method that eliminates all external optics and miniaturizes an entire multiplexed fluorescence system into a $2 \times 1\text{mm}^2$ chip through co-integration for the first time of massively scalable nano-plasmonic multi-functional optical elements and electronic processing circuitry realized in an industry standard complementary-metal-oxide semiconductor (CMOS) foundry process with absolutely 'no change' in fabrication or processing. The implemented nano-waveguide based filters operating in the visible and near-IR realized with the embedded sub-wavelength multi-layer copper-based electronic interconnects inside the chip show for the first time a sub-wavelength surface plasmon polariton mode inside CMOS. This is the principle behind the angle-insensitive nature of the filtering that operates in the presence of uncollimated and scattering environments, enabling the first optics-free 96-sensor CMOS fluorescence sensing system. The chip demonstrates the surface sensitivity of zeptomoles of quantum dot-based labels, and volume sensitivities of $\sim 100\text{fM}$ for nucleic acids and $\sim 5\text{pM}$ for proteins that are comparable to, if not better, than commercial fluorescence readers. The ability to integrate multi-functional nano-optical structures in a commercial CMOS process, along with all the complex electronics, can have a transformative impact and enable a new class of miniaturized and scalable chip-sized optical sensors.

© 2018 Optical Society of America under the terms of the [OSA Open Access Publishing Agreement](#)

1. Introduction

Fluorescence-based affinity-sensing is one of the dominant and the most powerful analytical tool especially for its unparalleled sensitivity, robustness, and specificity for the detection of proteins, DNAs, cells, toxins, bacteria, microorganisms, bioagents, and toxins in water, blood, food, aerosols and other media [1–3], including its use in single-cell analysis [4], in-situ hybridization [5], imaging [6–9] and in brain mapping [10]. For bio-molecules, classical affinity-based sensing (the current gold standard for proteins being Enzyme-Linked Immunoabsorbent Assay (ELISA)) consists of immobilized probes on the sensing platform and detection is achieved with fluorescence reporters. Extreme miniaturization of complex, versatile fluorescence-based biosensing platforms with massively multiplexing capability into pill-sized single-chip modules requiring only μW - mW levels of power can enable a wide range of new sensing modalities in-vitro and in-vivo [11–14], including real-time micro-biome analysis, distributed sensor networks for brain imaging [15], and microscale robots in blood for chemical analysis and drug delivery [16, 17]. This has been a long-standing challenge in neurobiology, nucleic acid and protein assay technology, primarily because high sensitive fluorescence detection ($\sim \text{pM}$) in presence of excitation signal (60-80 dB higher) in a multiplexed fashion requires complex optical set-ups

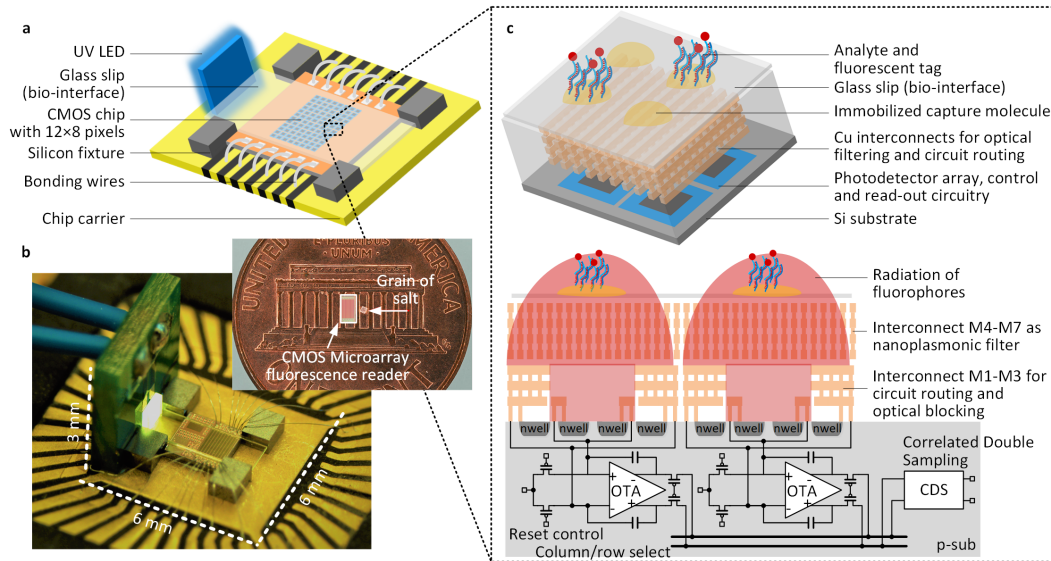


Fig. 1. Ultra-miniaturized CMOS fluorescence microarray system. **a**, Overview of the system including the CMOS IC with the integrated 96-sensor array, the UV LED as the excitation light source, removable glass slip as the bio-interface, and silicon fixtures enabling automatic alignment with a disposable bio interface for multiplexed detection. **b**, Fluorescence reader system. **c**, Perspective and cross-sectional view of the sensing pixels. The strong UV light excites the immobilized fluorophores to emit a weak signal in NIR. Integrated nanoplasmonic filter rejects the UV light and allows the local fluorescence to be detected and process by the photon-detection circuitry and integrated electronics underneath. The nanoplasmonic filter is realized using the 4th to 7th copper interconnect layers in the 65-nm CMOS process and spreads across all the sensor sites. The 1st-3rd interconnect layers are used for circuit routing and optical blocking. The multiplexed fluorescence signals are read out in a time-multiplexed fashion and are further processed by CDS circuits to eliminate random offsets and suppress low-frequency noise.

which are extremely challenging to miniaturize. Achieving such levels of sensitivity requires precise collection and low-noise detection of the fluorescence signals after filtering through an array of bulky optical components including excitation, dichroic and emission multi-layer filter sets, lenses and objectives arranged in collimated optics, often with motorized stages for scanning and reading [18]. The complexity of this limits the multiplexing ability of many lab-on-chip devices without significantly sacrificing sensitivity for fluorescence detection [19]. Prior efforts to miniaturize such fluorescence sensing systems have primarily relied on more compact ways to package these traditional components to enable applications in microscopy [20], sequencing [21] and fluorescence endoscopy [22]. This approach is fundamentally limited in the extent of possible miniaturization without significantly affecting sensitivity and multiplexing ability.

In this pursuit, CMOS provides a potential platform and over the last decade, CMOS and hybrid silicon systems have played a crucial role in high-precision sensing arrays in electrical detection of DNAs [23,24], DNA sequencing [25,26], nuclear magnetic resonance detection [27], electrochemical sensing [28], detection of redox-active metabolites in biofilms [29], in multiplexed electrophysiological recording of a large network of electrogenic cells [30–32] and in magnetic-based sensing [33, 34]. For fluorescence assays, while CMOS can enable high-density multiplexed photo-detection and readout with sensitivity comparable to CCDs, it does

not have the capability to manipulate optical fields to emulate the functions of the external optical components in a traditional fluorescence reader. This typically requires a similar approach as before with external filtering and collimating optics and post-fabrication [35–37], or by allowing fluorescence lifetime detection with complex laser synchronization with picosecond levels of accuracy [38, 39] and significantly sacrificing sensitivity (\sim nM).

Here, we report for the first time realization of massively parallelized nanoplasmonic optical structures and co-integration with electronic circuitry in a commercial CMOS integrated circuit (IC) with no custom fabrication or post-processing that allows us to eliminate all external optics, filtering, collimation or bulky lasers and enable full integration of 96-sensor fluorescence platform and reader system into a total volume of less than 0.1 cc. The co-integration of the scalable nanoplasmonics and electronics in the same substrate is demonstrated allowing optimal detection and filtering across the optical and electronic partitions enabling us to reach surface sensitivities of the order of zeptomoles ($\sim 1 \text{ dot}/\mu\text{m}^2$) of labels on the chip surface. This corresponds to surface density where less than 1 out of 1-100 million excitation photons gets converted into a fluorescence photon.

Exploiting metallic nanostructures to engineer optical fields has enabled significant progress in the field of metal-optics and nanoplasmonics in enabling sub-diffraction waveguiding [40, 41], nanofocusing [42, 43], plasmon modulation [44], flat lenses with meta-surfaces [45, 46], and plasmon resonance-based enhancements for Raman spectroscopy and biosensing [47–49]. In spite of the progress, the application of such plasmonic structures have been limited due to their use as only discrete optical components, and their fabrication in custom lithographic processes using noble metals making them incompatible with CMOS fabrication [50]. *To enable the multiplexed assay and massively parallelized nanoplasmonic elements with integrated electronics, we adopted an absolutely ‘no change’ approach to the CMOS fabrication and demonstrate this system in an industry standard 65-nm process, typically used for microprocessors and wireless ICs.*

While our prior proof-of-concept work has shown the ability to integrate one sensor in silicon to detect fluorescent tags (not labeled bio-molecules) on the chip surface with an external laser with moderate sensitivity [51], the presented work demonstrates scalable complex nanoplasmonic-electronic systems for massively multiplexed assays in CMOS, allowing the entire system miniaturization including an uncollimated optical LED source. The multiplexing capability is key element for all medical diagnostics, critical for screening and for allowing multiplicative readouts from a single assay, including the blank control, to significantly improve the statistics and reducing the false-positive and false negative rates. In addition, we show its ability to operate with a side-positioned excitation LED (which is key for extreme miniaturization and low power operation), improve the sensitivity of each pixel by 70 fold reaching that of commercial benchtop readers and demonstrate the detection of both proteins and nucleic acids with the assay chemistry on-chip in a multiplexed fashion. *More importantly, this work demonstrates that such co-design and co-integration of electronics/nanoplasmonics in a single substrate allows tighter control of the optical path and can overcome partial limitations of any one component through cross-layer optimization.* As an example, the multiple distributed control sites allow us to sense the average residual background and filter it through a combination nano-optical filtering upfront (45-60 dB) and subsequent electronic filtering to achieve an end-to-end excitation-to-fluorescence sensing capability of $P_{ex}/P_{fl} \approx 77 \text{ dB}$ for a signal-to-noise-ratio (SNR) ≈ 1 , enabling $\sim 100 \text{ fM-pM}$ levels of assay sensitivity comparable to, if not better than, commercial optical DNA microarrays [52, 53] and ELISA systems [54]. With the integration capability CMOS, the technology can be potentially scaled into tens of thousands of sensor sites, if not hundreds of thousands [55–57].

2. Experimental method

2.1. System architecture overview

The fluorescence microarray system consists of the CMOS chip with the integrated filters, detection, read-out and signal processing circuitry, UV LED source and carefully placed tiny silicon-wafer based fixtures that allows automatic alignment with a disposable functionalized glass slip (bio-interface) for multiplexed detection (Fig. 1(a)). A vertically positioned low-cost UV LED serves as the excitation light source. The light is incident from near grazing angles to the surface of the glass slip and is rejected by the angle-insensitive nanoplasmonic fluorescence emission filter integrated inside the sensor chip. The NIR emission from the spatially multiplexed fluorescent tags, on the other hand, passes through the filter efficiently, gets detected by the photo-detector arrays and electronically processed by the IC. The chip measures $2 \times 1\text{mm}^2$ ($\sim 1.4\text{mg}$) and the entire sensing part of the system (including the excitation light source, the sensor IC, the fixtures and the bio-interface) occupies a volume of around 0.1cc, as shown in Fig. 1(b). Due to the elimination of all external optics, filtering of the excitation light is critical to robust operation of a fluorescence sensor array. As shown in the perspective and cross-sectional view in Fig. 1(c), the filter and the interconnects are co-designed with the embedded copper layers in the 65-nm CMOS process. Each of the 96 pixels comprises of 80/80 differential photodiodes laid out in a symmetric fashion, with a capacitive trans-impedance amplifier (CTIA). The signals are readout in a multiplexed fashion and are further processed by the correlated double sampling circuits to suppress random offsets and low-frequency noise. The co-design and integration of optics, electronics and bio-chemistry in one platform allows strict control of the entire process from optical transduction to sensing data extraction.

2.2. Integrated angle-insensitive nano-plasmonic filter in CMOS

In a classical fluorescence set-up, both fluorescence signal and laser excitation are collimated to allow the usage of a high-performance multi-layer fluorescence emission filter which typically works within a very small range of angles ($\approx \pm 5^\circ$) [35, 36]. In this miniaturized sensor platform without optical collimation, the radiation from the fluorescent dipoles on the surface interacts with the integrated filters in a complex fashion for a wide range of incident angles [58–60]. This is shown in the simulated radiation propagation (originated from the dipole location) for random polarized fluorescent emitters at the air/SiO₂ interface (Fig. 2(a)).

In addition, the filter needs to handle the near-grazing excitation light as well as the scattered light from the assay and other necessary structures of the CMOS chip (e.g. the bonding pads). Therefore, the angle insensitive characteristic of the filter with rejection ratios ($\geq 40\text{dB}$) becomes a critical and differentiating factor to enable chip-scale fluorescence sensing. This precludes any resonant filter structures, such as interference-based or resonant plasmonic coupling [61, 62] or classical grating structures implemented in CMOS [63]. In this work, we exploit the fundamental loss of plasmonic waveguiding in copper to enable angle-insensitive filter characteristics.

In the 65-nm industry standard CMOS process, the lowest metal layers in close proximity to the transistors have the smallest feature sizes ($\approx 100\text{ nm}$ width, $\approx 130\text{ nm}$ spacing). The nanoplasmonic filter is designed to be an array of vertical nano-slab waveguides realized with the 4th – 7th copper interconnect layers and the via layers in between, in total measuring $1.41\ \mu\text{m}$ in vertical length in the direction of the optical mode propagation (Fig. 2(b)). Electronic signals are extracted from the photon-detection circuitry underneath the filter and transferred to the edge of the chip using the 1st – 3rd interconnect layers. The entire optical path, filters and the electronic routing are co-designed to ensure optimal performance and to minimize scattering light leakage from the sides of the chip. When excited with the randomly oriented fluorescence tags from the surface of the chip and the excitation signal, the sub-wavelength nano-plasmonic filter channelizes a collection of modes including coupled surface plasmon polariton (SPP)

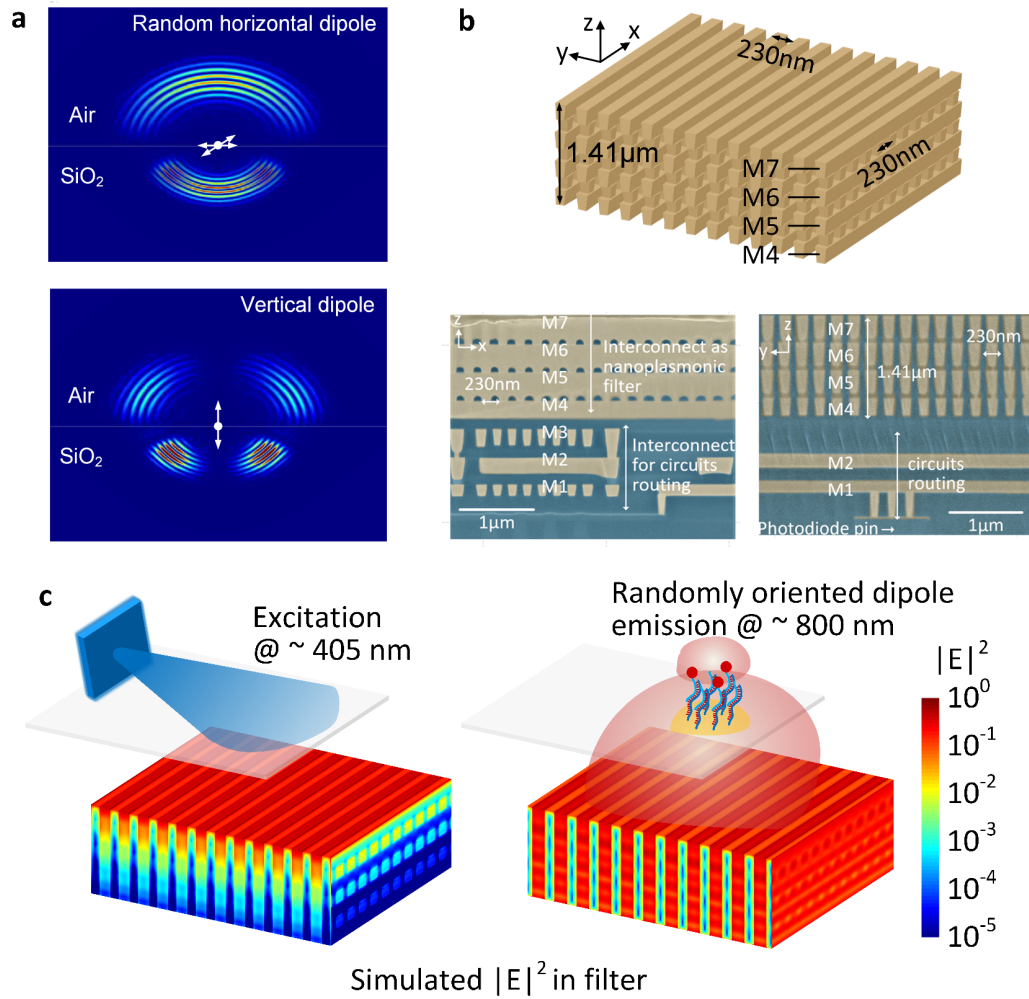


Fig. 2. **a.** Simulated radiation propagation (originated from the dipole location) for randomly polarized fluorescence emitters on the chip surface at the air/SiO₂ interface. **b.** Structure and SEM image of the integrated nano-plasmonic filter, implemented in 65 nm CMOS process with minimum metal linewidth of 100 nm and spacing of 130 nm. **c.** The simulated electric field intensity in filter for LED excitation at 405 nm and fluorescence emission demonstrates the angle-insensitivity of the nanoplasmonic filters with nearly 50 dB of optical filtering.

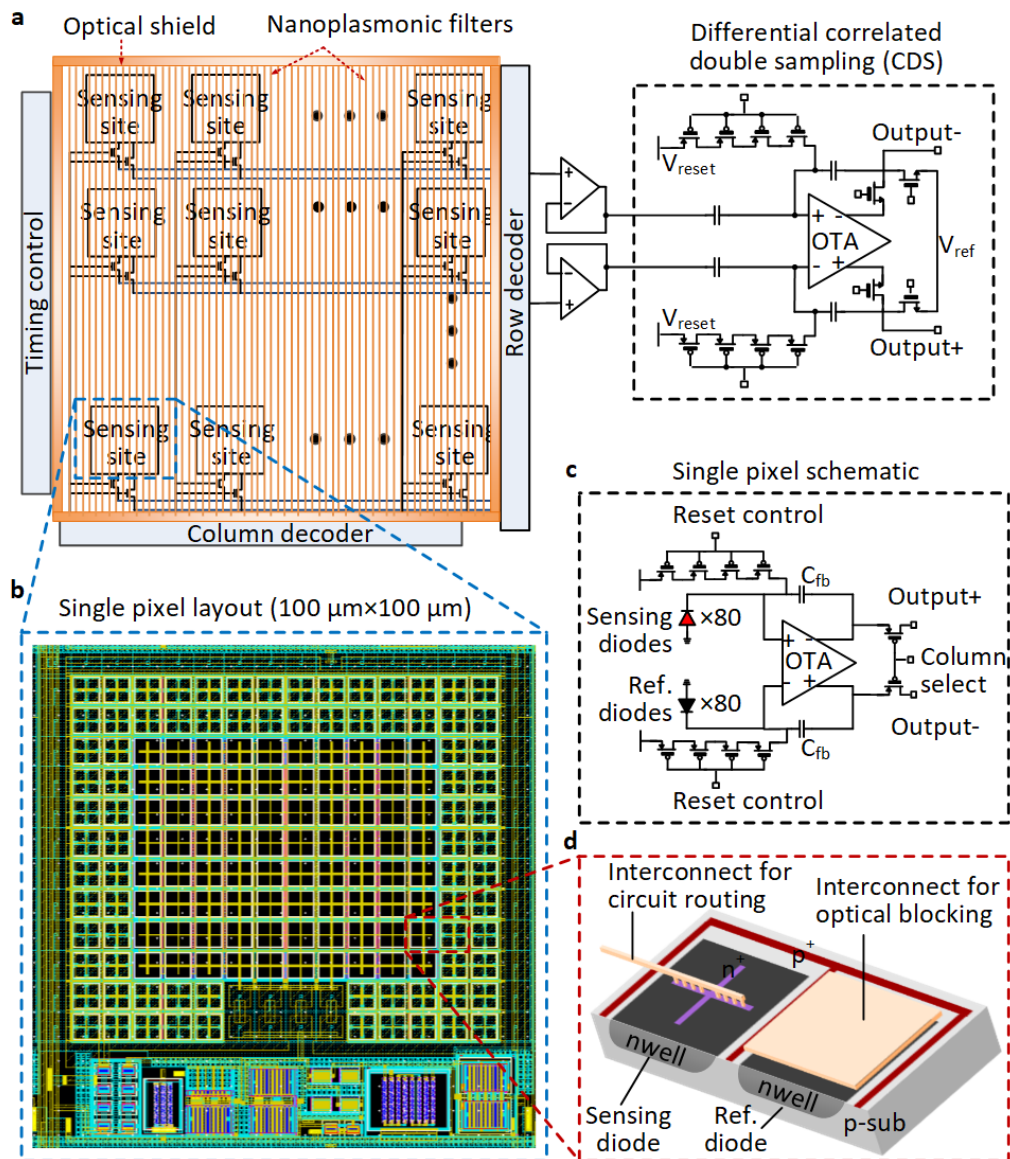


Fig. 3. **Circuit architecture.** **a**, Circuits architecture of the 96-sensor array chip with the integrated pixels, control and readout circuitry, nanoplasmonic filters and optical shield, all co-designed in a single IC. **b,c,d**, Layout and schematic of a single sensing pixel. The photo-detection is enabled in each pixel with 80 sensing diodes at the center measured differentially with respect to symmetrically placed and shielded 80 reference diodes to suppress common-mode dark currents. The signals are processed with differential CTIA. Each photodiode is implemented using nwell-psub structure and each pixel measures $100\ \mu\text{m}$ in each dimension.

modes and coupled cavity modes. Complete removal of all external collimating optics for true miniaturization requires the angle insensitivity nature of the filter operation. The work leverages the sub-wavelength spacing of the array to ensure that the cavity modes are largely suppressed and the plasmon modes are dominant in the waveguide system. As the coupled SPP modes propagate, the modes exploit the inter-band transition of copper near the excitation wavelength at 405 nm to absorb the light while the SPP modes at the fluorescence wavelength propagate with high efficiency to get collected and processed by the integrated electronic circuitry. The core principle of background suppression in this multi-modal nanoplasmonic filter is through the differential losses of the coupled SPP modes across the two wavelength regimes enabling nearly 35 dB/ μm of rejection ratio per 1 μm of vertical wave travel. Therefore, simply the lowest three metal layers measuring 1.41 μm in length enables 50 dB of optical filtering as shown in the simulated optical fields inside the filter in Fig. 2(c). Collectively, when combined with electronic filtering at the backend, the system achieves an end-to-end filtering capability reaching up to 77 dB. The LED excitation can be at any angle of convenience, and the choice of near-grazing incidence from a side-positioned LED in this work is to preserve the ultra-compact packaging of the system. The complete and theory, modal analysis, band structure, full-wave simulation, and experimental result of the nano-plasmonic filter can be found in [64]. Other examples of nano-optical systems in CMOS can be found in [65–70].

2.3. Integrated circuits, read-out and signal processing

The architecture of the custom CMOS chip consists of an array of 96 sensing pixels with multiplexing and CDS readout circuitry, and a sheet of nanoplasmonic fluorescence emission filter to reject the excitation background (Fig. 3(a-d)). Each sensor size is kept at $100 \times 100 \mu\text{m}$ in accordance with commercial DNA/protein arrayer for multiplexed assay on the surface. However, in principle, the sensor sizes can be reduced at least by a factor of 100 in area enabling tens of thousands of sensing sites for massively multiplexed assays and imaging. The entire chip is surrounded by the vertical optical shield, which is also made by the copper interconnects similar to the nanoplasmonic filter, that suppresses leakage of scattered light into the chip sensing sites from the side edges. In order to minimize the effect of dark current and increase sensitivity, photo-detection is enabled in each pixel with 80 sensing diodes at the center measured differentially with respect to symmetrically placed and shielded 80 reference diodes (Fig. 3(b)). The differential signal processing also exploits the correlation in diode dark currents. This fluctuation in temperature, LED power and voltage supply across the sensor and reference sites suppresses these variations as common mode allowing high sensitivity detection.

2.4. Multiplexed assays and sensor cross-talk

The sensor array design needs to take into account the cross talk between the pixels for multiplexed assays. The mutual coupling of the fluorescence signal from localized spots to the neighboring pixels is dependent on the assay interface with the sensor. The CMOS chip surface is typically coated with silicon nitride layers, and functionalization can be done on a 1 μm thick glass grown on the surface [33]. Fig. 4(a-c) shows the set up and electromagnetic simulation of fluorescence dipoles spread on a 50 μm spot size on the 1 μm thick glass surface on the chip. The labels mostly radiate into the chip and as can be seen, the lateral spread is kept to a minimum and almost fully confined to the local pixel underneath minimizing cross talk. The primary reasons to choose the pixel size to be 100 μm is to enhance this light collection efficiency and minimize cross talk and keeping in line with commercial arrayers that can allow spot sizes to be confined between 50-75 μm . In a commercial setting, this is an appropriate methodology since the low-cost chip can allow one-time disposable use. In the laboratory setting, to reuse the same chip for multiple bio measurements, we design a disposable functionalized glass slip (also shown in Fig. 1), which is supported by silicon positioners to allow easy alignment with

the on-chip sensor array. The glass slip is held approximately $100\ \mu\text{m}$ from the chip surface as shown in Fig. 1 and Fig. 4. Evidently, this causes spreading of the fluorescence emission from the localized spots into the sensor array resulting in cross-talk among the neighboring pixels. While this limits the number of spots we can perform on the surface with this particular glass slip set-up, this packaging is only used for chip reuse. The functionalization on a thin glass grown on the chip surface has been shown in [33] and can be performed on the presented chip as well.

3. Results

3.1. Integrated nanoplasmonic filter performance

The optical filters are characterized with the integrated photo-detectors. Fig. 5(a) shows the measured normal incidence transmission spectrum (normalized) for the y -polarization (perpendicular to the slabs). To comply with the design rule checks of the CMOS fabrication process that ensure high yield, the filter is designed to allow light to pass for one polarization along y . The sub-wavelength spacing blocks all wavelengths for the other polarization and therefore, the system requires no external polarizer for the LED light source. The only effect of this is that the yield of the photon detection is reduced by half. We choose quantum dots as the fluorescence tag in this case for their photo-stability, stronger emission and higher Stokes shift [76]. Fig. 5(a) shows fluorescence excitation and emission spectrum of the chosen Qdot 800 fluorescent tag that matches with the filter performance [70].

Fig. 5(b) shows the measured responsivity ratio (in dB) between fluorescence at 800 nm and excitation at 405 nm wavelengths, demonstrating an average filtering ratio of 45 dB achieved for the center 4×10 pixels. The remaining pixels on the side suffer from additional optical leakage at 405 nm, due to μm -sized gaps needed to comply with design-rule-checks for the CMOS process as the electronic signals are routed to the edge of the chip through the shield. As seen in Fig. 1, the chip is unpackaged and exposed to all forms of scattering and standard optical packaging can suppress this additional leakage.

Fig. 5(c) and Fig. 5(d) show the measured filter transmittance (normalized) for the excitation and emission wavelengths across angles of incidence and polarizations, demonstrating rejection ratios varying between 45-60 dB. In essence, the subwavelength non-resonant nature of the nanoplasmonic structure ensures the rejection of near-grazing or scattered excitation light from all angles, which is critically important for sensitive bio-molecular assays. This allows us to eliminate collimation, objective lens and other external optical filtering elements and replace the typical excitation laser by an ultra-compact low-cost LED for an overall ultra-miniaturized system.

3.2. Microarray alignment for multiplexed detection and disposable interface

In practical applications, while the mm-sized biosensor chip platform with the LED and silicon fixtures may serve as the sensing platform, the functionalized glass cover slip can serve as the removable and disposable cartridge for multiplexed sensing. Since the interface is spotted with the probes and placed on the CMOS chip, it is very important to ensure that the capture spots are accurately aligned with the sensors on-chip. This is ensured by four silicon fixtures that clamp on the glass slip when simply placed on the chip, thereby accurately aligning the spots with the sensors.

As shown in Fig. 6(a), the four tiny silicon-wafer based fixtures are placed to fit the size of the cover slips with estimated gap being $5\text{-}10\ \mu\text{m}$, and each glass cover slip is precisely diced to have near-identical dimension. In order to perform multiplexed detection of DNA on the same cover slip, multiple capture DNAs have to be printed precisely on different sensor spots, requiring alignment of the DNA arrayer/printer with sensor pixels. The alignment is performed in the following way. Firstly, the distance between the top left corner of the cover slip (x_0, y_0) and a

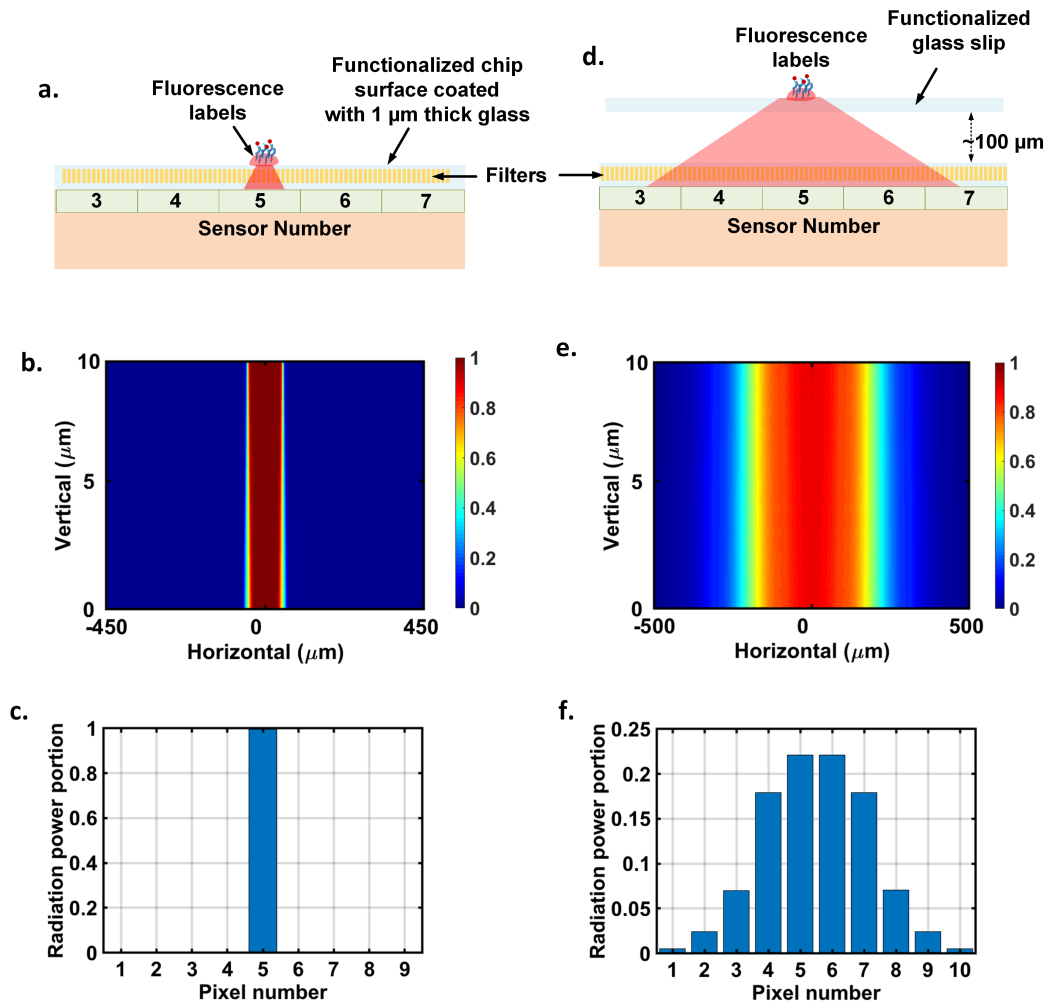


Fig. 4. **Sensor cross talk on the multiplexed assay based on the bio-interface.** **a.** Assay can be performed directly on a functionalized 1 μm thick glass grown on the chip surface. **b,c.** Electromagnetic simulation of the fluorescence emission from a 50 μm diameter spot on the surface and its coupling in the lateral dimensions. Since the pixels are 100 μm in dimension, the emission remains localized to the pixel underneath the spot minimizing cross-talk. **d.** To re-use chip to do multiple measurements in a laboratory setting, we create a disposable bio-interface that is aligned with the sensor array with silicon positioners (Fig. 1). We perform the experiments on the glass slip positioned about 100 μm from the chip surface. **e,f.** Electromagnetic simulation of the fluorescence emission from a 50 μm diameter spot on the glass slip. The elevation causes the emission to spread creating cross-talk among the neighboring pixels. This limits the number of spots we can perform on the surface and is only done to reuse the chip for multiple experiments in a laboratory setting. The functionalization can be done on the chip surface as shown in part **a.**, similar to [33].

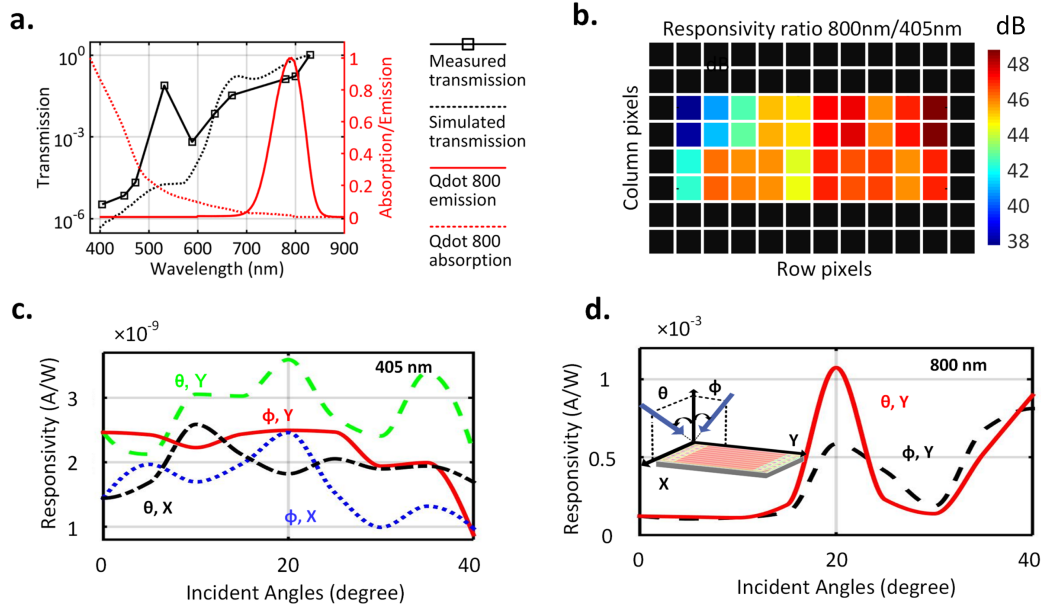


Fig. 5. **a.** Measured (and simulated) transmission spectrum (normalized) showing ~ 47 dB rejection ratio between 800 nm and 405 nm wavelengths. The absorption and emission spectrum of the chosen quantum dot fluorophore (Qdot 800) are shown inside the figure. **b.** Measured filtering ratio (in dB) for emission and fluorescence shows an average ratio of 45 dB for the center 40 pixels. **c,d.** Measured transmission at excitation and fluorescence wavelengths with varying incident angles and polarizations. **e.** Using on-chip decoders to address the sensor array and read out multiple pixels within single integration (200 ms). **f.** Measured sensitivity shows capability of detection of fluorescence signals, 77 dB below the excitation.

reference point of the sensor array (x_1, y_1) is measured using a microscope and a 2D translational stage. Since each pixel on the sensor (x_i, y_j) with respect to the reference point (x_1, y_1) is known (the pixels have fixed pitch $p = 100\mu\text{m}$), the distance between the pixels and the top left corner of the cover slip is therefore:

$$d_x = x_1 + (i - 1)p - x_0 \quad (1)$$

$$d_y = y_1 + (j - 1)p - y_0 \quad (2)$$

where $i=1, 2, \dots, 8$, and $j=1, 2, \dots, 12$ represent the column and row number of the 96 pixels. When the multiple DNA capture strands are printed, the pin of the arrayer is aligned to the top left corner of the cover slip (x_0, y_0) first, and subsequently travels a small distance of (d_x, d_y) to print on the point of the cover clip that is well-aligned with the related pixels. Such calibrating method, where the travel distance (d_x, d_y) is in mm range, minimizes the alignment error and therefore maximizes the repeatability of the multiplexed detection scheme of the sensor. The overall accuracy in spotting which includes the gap between the glass slip and the fixture, and the accuracy of the spotter is estimated to be less than $10\mu\text{m}$. This is much smaller than a single sensor size of $100\mu\text{m}$, and therefore signal cross-talk is minimized.

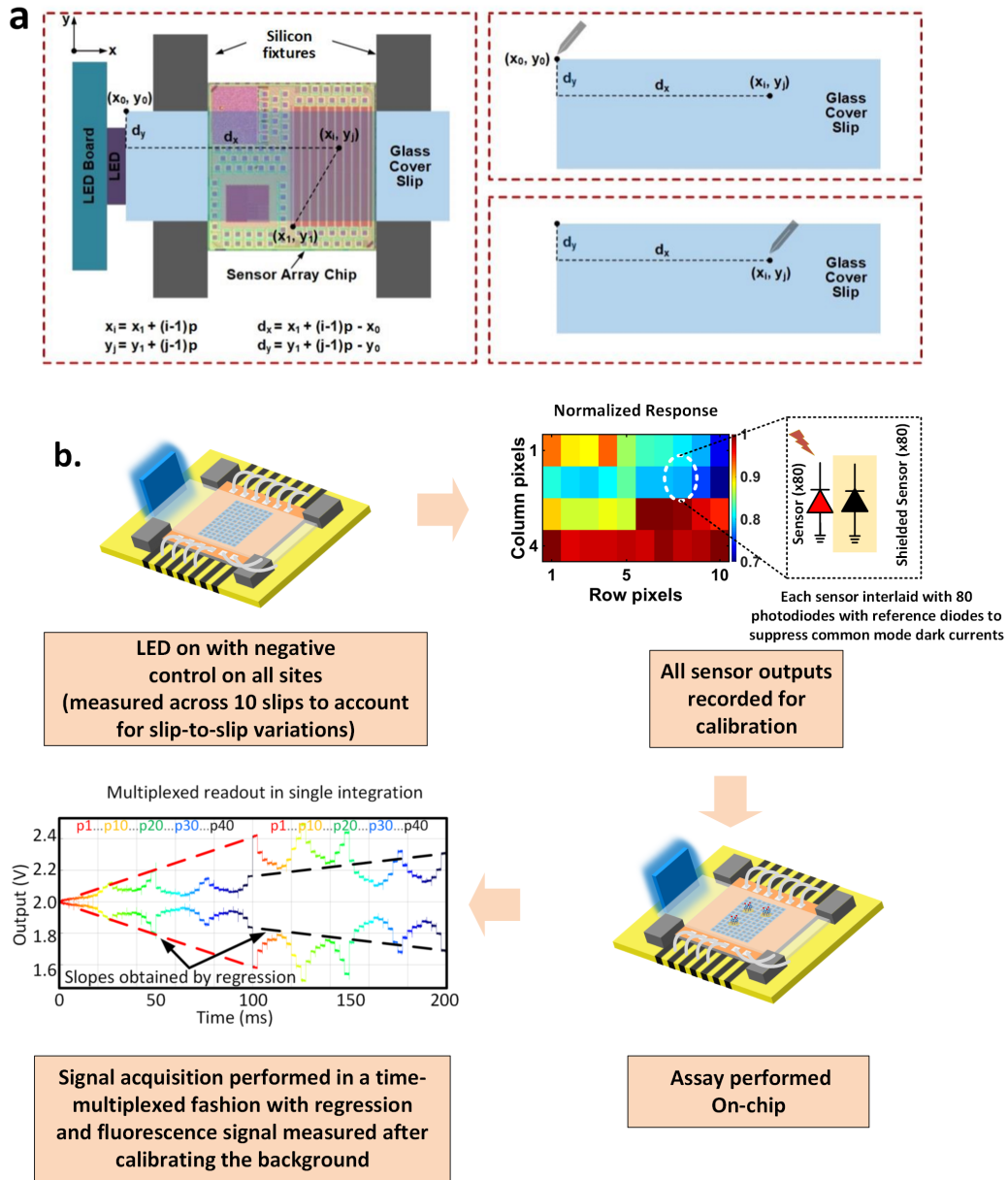


Fig. 6. **a**. Alignment of the bio-interface (glass slip) with the sensor array for multiplexed assays. **b**. Calibration process and signal acquisition for the assay.

3.3. Sensor array calibration, read-out and sensor noise

In the 96-multiplexed sensor array, each sensing site processes the local emissions of the fluorescence signal on the glass slip above and provides a differential signal at the output when addressed electronically. The side positioned LED minimizes direct incidence of light on the chip surface that reduces leakage. This allows a higher integration time that enhances sensitivity, as we will show later in the paper. We measured the light intensity on the glass slip and it averages approximately 0.2 mW/mm^2 that translates to nearly 70% of the power being incident on the assay. While this is fairly efficient, the coupling efficiency can certainly be improved with a tighter control of the light path.

The method of sensor calibration and assay read-out is shown in Fig. 6(b). There is expected sensor-to-sensor variation due to the differences in responsivity of the photodiodes, filter rejection ratio and due to differences in impinging excitation light from the side-positioned LED. All of these collectively are measured for a one-time calibration with 10 different cover slips with negative control on all sites. This is done to average out the variations in the scattering effects of the functionalized slips. The measured average response of the center 40 pixels under this condition is shown in Fig. 6(b). The average spatial variation across the pixels remains within 1 dB and the slip-to-slip variation is less than 0.3 dB. This is a one-time calibration process that is common to many commercial electronic chipsets where during the testing phase, sensors are calibrated automatically with a source, and the results are stored in a memory. In fact, this can be automated with built-in self testing mechanism where the LED can be switched on by the system periodically and the sensor can be recalibrated. The disposable bio-interface now can allow the same sensor and reader interface to be reused for other assays.

With on-chip column and row decoders, there are many possible ways to extract the signals from the pixel array. Fig. 6(b) shows one such scheme, which resets and activates all the sensor sites at the same time and reads the signals in a time-multiplexed fashion in one single integration period. As an example to read the center 40 pixels, each of the sensors are read twice within one integration period (e.g. 200 ms). This is shown in Fig. 6(b), where each color represents the measured waveform of one pixel. In this way, we obtain two short signals separated by around 100 ms for each pixel (different pixels are plotted in different color in the figure). Regression analysis can be subsequently performed on the two shorter time series to obtain the pixel integration slope which is proportional to the light power. As an example, the two short time series at around 0 and 100 ms (marked by red color denoting the signal for pixel 1), is regressed with the red line. Likewise, the two short black time series at 100 ms and 200 ms (denoting the signal for pixel 40) is regressed with the black line (Fig. 6(b)). Such readout scheme keeps the total readout time short to allow the use of averaging for noise reduction with 100 acquisitions in less than one minute. The slope of the output signal is approximately given by $V_{sig}(t) = \frac{i_{ph}t}{C_{fb}}$, where i_{ph} is the photo-current and $C_{fb} \approx 15.6 \text{ fF}$ is the feedback capacitor (Fig. 3(c)) across which the signal is integrated. In a typical operation, the total light power is $\sim 2.4 \text{ pW}$. With the photodiode quantum efficiency being Q.E. ~ 0.1 , $i_{ph} \approx 156 \text{ fA}$, the signal can be integrated for 100 ms for maximum swing voltage of $V_{sw}=1 \text{ V}$.

Expectedly, the SNR of the sensor is mainly determined by the filter performance, fluorescence intensity and the noise of the sensor, which includes the circuits noise, and mainly the photon shot noise upon fluorescence excitation. The average noise voltage in dark ($V_{n,dk}$) is around 0.51 mV. In fluorescence excitation, the total sensor noise increases with integration time reaching a maximum value of $V_{n,ph} \approx 3.5 \text{ mV}$ (where the shot noise alone $\approx \sqrt{\frac{eV_{sw}}{C_{fb}}} \approx 3.2 \text{ mV}$). It should be noted that given the excitation and fluorescence light power, $V_{sig} \propto t$ and $V_{n,ph} \propto \sqrt{t}$, and therefore, $SNR \propto \sqrt{t}$. Therefore, the maximum integration time reaching full voltage swing should be used to increase SNR. With the proposed time-multiplexed reading scheme, multiple signal acquisition can be performed within a reasonable time period ($< 1 \text{ min}$) to reduce the total

noise from 3.5 mV to 0.7 mV through averaging.

3.4. Coverslip functionalization

The tiny glass slips that serve as the bio-interface are placed and temporarily fixed inside glass wells with volume around 300 μL , in which the DNA hybridization and protein sandwich assays are performed. To minimize nonspecific binding of biomolecules and Qdot fluorescent tags, the surfaces of the glass slips are passivated and functionalized with reactive chemical groups to attach the capture molecules. All steps are performed at room temperature unless otherwise specified. The glass wells and the glass slips are first washed in 1 M KOH solution for 2 hours, and then rinsed thoroughly with Millipore water. For DNA detection, subsequently, the glass slips are incubated for 15 minutes with a mixture of BSA and Biotin-BSA in Tris-NaCl buffer, with the concentration being 5 mg/ml and 0.1 mg/ml, respectively. Then the wells are rinsed 5 times with Tris-NaCl buffer. After that, the glass slips are incubated for 20 minutes with 10 mg/ml streptavidin (ProspecBio) in 0.2 mM PBS buffer, and rinsed again with Tris-NaCl buffer. For protein detection, after the same KOH cleaning, the glass slips are rinsed with ethanol and incubated in 2% (3 glycidyloxypropyl)trimethoxysilane (Sigma-Aldrich) in 95% ethanol for 30 minutes. Afterwards, the glass slips are rinsed with ethanol, dried with N_2 , and baked at 110° for 15 minutes to improve the attachment of silane groups to glass surface.

3.5. Biosensing experiments

For DNA hybridization assay, immediately after the streptavidin incubation and washing, the glass slips are incubated for 15 minutes with biotinylated capture DNA strand (IDT) of 500 μM concentration in PBS, and then they are rinsed with PBS buffer. The capture DNA (Biotin-5'TTTTTTTTTTTTTTTTTGGCCCTACGCGTGAC3') has 33 bases. After that, the glass slips are incubated for 15 minutes with various test concentrations of 100 μL target DNA (3'CGGGATGC-GCACATGTTTTTTTTTTTTTTTTTTT5'-Biotin and/or other non-complementary sequences for negative control), diluted from stock solution in PBS with 0.05% Tween20 (Sigma-Aldrich), which is a surfactant used to suppress non-specific binding on surface. After rinsing the glass wells with PBS buffer, the glass slips are incubated for 15 minutes with 1 nM Qdot 800 streptavidin-conjugates, diluted from stock solution in PBS with 0.05% Tween20. The glass wells are then thoroughly washed in PBS for 8 times to remove the unbounded fluorescent quantum dots, and the cover slips are removed from the wells to be measured on top of the sensor chip. For DNA microarray experiments, instead of incubating the entire glass slip with the same capture DNA, we use a commercial microarrayer (XactII from LabNEXT) to print different capture DNA strands on different spots of the glass slip. Then various mixture of DNA targets are tested. Other steps are identical to single DNA hybridization assay. For protein detection, we use human IL-6 protein (Biolegend) as an example for demonstration. The capture antibody and detection antibody of IL-6 will both specifically bind to different parts of IL-6, respectively (both are from Biolegend). After the silane functionalization of the glass slips, the Human IL-6 capture antibody ($\approx 0.4\text{mg/ml}$) is incubated with the prepared glass surface overnight at 4 °C. The glass slips are then rinsed with washing buffer (0.05% Tween20 in PBS) and incubated for 2 hours with 100 μL target solution (IL-6 and/or IFN- γ for negative control) of various test concentrations, obtained from stock samples dissolved in PBS with 1% BSA. The cover slips are rinsed 8 times with the washing buffer and subsequently the human IL-6 detection antibody ($\approx 60\mu\text{g/ml}$, biotinylated) is applied and incubated for 1 hour. The glass slips are then rinsed with washing buffer and immersed with 1 nM Qdot 800 streptavidin conjugates for 15 min. The glass wells are then thoroughly washed in washing buffer for 8 times to remove the unbounded fluorescent quantum dots. The cover slips are removed from the wells to be measured on top of the sensor chip.

3.6. Limit of detection of quantum-dot based fluorophore

The ability to detect extremely low level of fluorophores on the surface of the chip is crucial for the chip-scale fluorescence reader to be deployed in practical settings where the number of target analytes is limited. To quantify the performance of fluorescence biosensors, the minimum detectable surface density of fluorophores is one of the most direct metrics. In order to estimate this, a tiny droplet of quantum dot solution in water with $0.5 \mu\text{L}$ volume with certain volume concentration is dropped on the glass slip, let dry, and is subsequently placed on the surface of the sensor chip. The average surface density can be estimated by the liquid volume, volume concentration, and the surface area which is roughly a circle with radius around 0.5 mm . Different cover slips with varying Qdot surface concentration are measured upon LED excitation. At the lowest detection level, a volume concentration of 2.5 pM is used, resulting in an estimated surface density of $\approx 1 \text{ dot}/\mu\text{m}^2$, as shown in Fig. 7(a), with $\text{SNR} \sim 4$. In order to further verify the surface density, the same procedure is repeated on cover slips and is subsequently viewed under a fluorescence microscope. Fig. 7(a) shows a magnified portion of the fluorescence image. To quantify the density, a 2D peak search algorithm is employed on a large $180 \mu\text{m} \times 137 \mu\text{m}$ area of the fluorescence image divided into 9×9 sub-sections. The total number of quantum dots in each sub-section is calculated and divided by the sub-section area to calculate the distribution of the surface density. As shown in Fig. 7(a), the mean value of the surface density is $\sim 0.6 \text{ dot}/\mu\text{m}^2$. During the measurement, we record the middle two sensor data that has a moderately uniform surface density as captured in the fluorescence image. The image shown in the figure is spread over two pixels of the sensor. Therefore, the signal recorded from the sensor corresponds to the fluorescence image in Fig. 7(a). This allows us to accurately calculate the surface density. This slightly lower number than the estimation of $1 \text{ dot}/\mu\text{m}^2$ from total number of molecules can be attributed to the increased density at the boundary of the droplet when it was dried. Note that the demonstrated ability to reach the surface densities of the order of $1 \text{ dot}/\mu\text{m}^2$ is equivalent to a total of 5 zeptomole (10^{-21}) molecules on the sensor surface (the active photo-sensing area is around $55 \mu\text{m} \times 55 \mu\text{m}$ for one pixel). This exceeds the surface sensitivity levels of modern fluorescence scanners and readers which are typically in the attomole range.

3.7. DNA and protein detection

Fig. 1 shows the system integration of the sensor array with the bio-assay interface. In order to be compatible with standard assay procedures, capture probes (nucleic acids/proteins) can be immobilized on a $100 \mu\text{m}$ thick cover slip ($1.3 \text{ mm} \times 5 \text{ mm}$) using a commercial micro-arrayer. This not only allows re-usability of the chip but also avoids deposition of glass required for immobilizing capture probes directly on the chip surface. The assay experiments are carried out in a glass well containing the cover slip and after completion of the procedure with the target/probe solution and fluorescence labeling, the test slip is placed on the chip surface for detection and analysis (Fig. 1). The signals from the sensor arrays are then electronically processed on chip for analysis. The platform can be functionalized with specific bio-probes with conventional micro-arrayer to prepare the disposable cartridges, i.e., the glass slip.

The chip is tested for both DNA and protein detection where the glass slips are placed in separate glass wells ($\approx 300 \mu\text{L}$ in volume) and standard assay protocols are subsequently performed. With target DNA concentration varied between 100 fM - 100 pM and allowed to hybridize with the complementary capture DNA, the composite is detected using a streptavidin-conjugated Qdot 800 fluorescent tag. The sensor output and the standard error for positive and negative control slips are shown in Fig. 7(b). The standard error is the standard deviation of the signals measured from multiple sample slides performed with the same assay procedure. Although the sensor noise is low, the functionalization itself has some variations across the slides so the error bar is primarily due to the variations in the assay chemistry. The chip demonstrates a linear response with limit of detection (LOD) of 100 fM at $\text{SNR} \approx 2$. For proteins, we measure

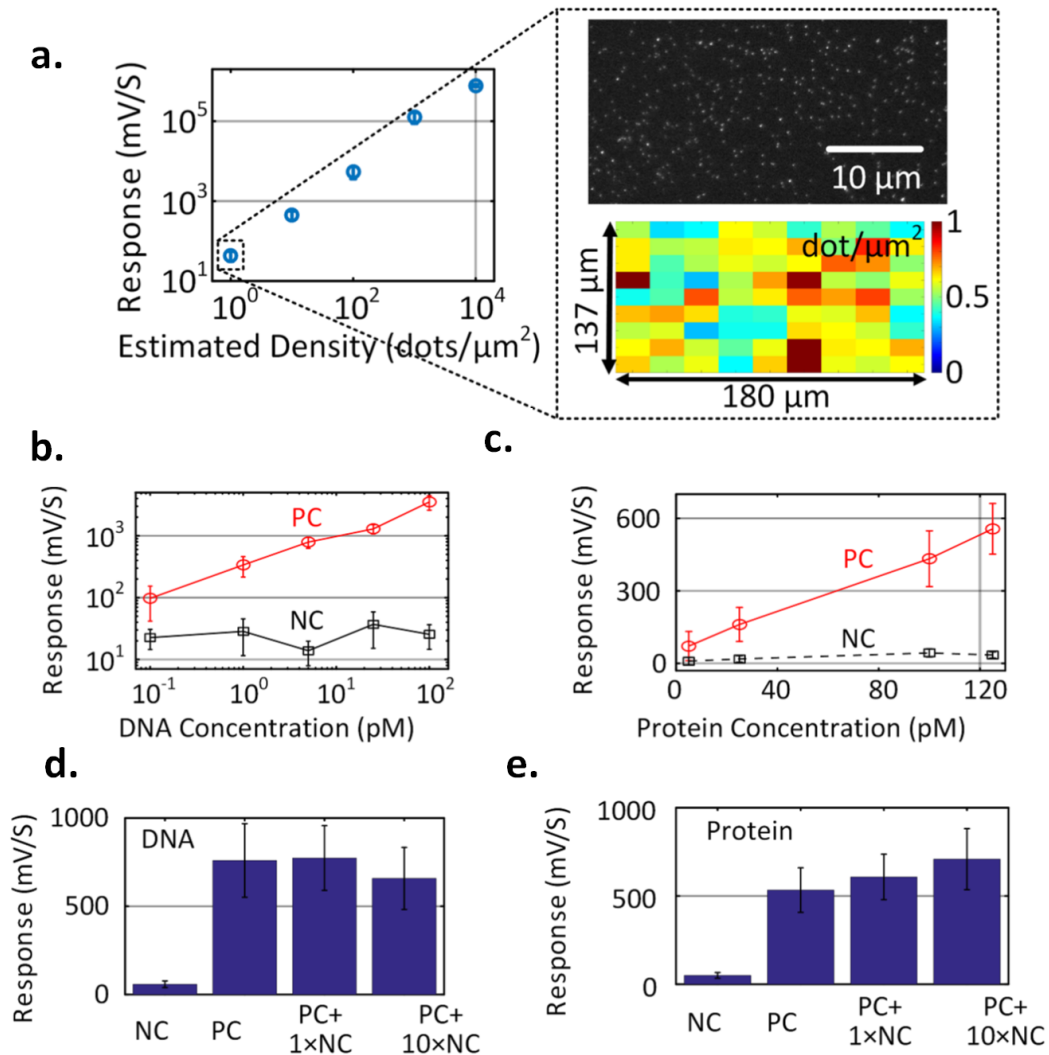


Fig. 7. Measured sensor response versus surface density of QD 800 fluorophore demonstrating sensitivity level below $1 \text{ dot}/\mu\text{m}^2$. The inset figure shows the distribution of surface densities captured in a fluorescence microscopy set-up corroborating with the average surface density. **c,d.** Measured sensor response against target volume concentration in DNA and protein (IL-6) assays, demonstrating volume sensitivity level down to 100 fM for DNA and 5 pM for protein. **e,f.** Measured effects of non-specific binding for target volume concentrations of 10 pM for DNA and 100 pM for IL-6.

the detection of human IL-6 which is a multi-functional cytokine playing critically important roles in the regulation of a wide range of biological activities in various cell types and in the auto-immune processes in many diseases. A sandwich assay for human IL-6 detection is carried out with human IL-6 capture antibody immobilized on the surface. The bio-interface is incubated with IL-6 target. A secondary biotinylated detection antibody is introduced for the sandwich assay and finally the streptavidin-conjugated Qdot 800 is introduced to serve as the fluorescent label. A linear response is demonstrated for target concentrations varying between 5-125 pM with the LOD being 5 pM (Fig. 7(c)). Fig. 7(d) and Fig. 7(e) show the effect of non-specific binding on both DNA and the assays. Specifically, varying concentrations of non-complementary DNA and nonspecific protein (*IFN- γ*) are introduced into their respective assays with fixed concentration of the target DNA (~ 10 pM) and target protein (~ 100 pM). As shown in the figure, the effect on the fluorescence signal is small and can be further suppressed with an optimized blocking agent.

3.8. Multiplexed nucleic acid detection

Fig. 8(a)-Fig. 8(c) shows the multiplexed detection capability of the sensor array with different DNA capture strands showing positive responses at the conjugated site and almost no signal at the non-specific sites. Multiplexed detection schemes need to take into account the cross-talk across the pixels. In this experiment, the spotted sizes of the capture DNAs are around 200-300 μm which are larger than the sensor size. Further, the glass slip being 100 μm away from the sensor, the fluorescence emission spreads to the neighboring pixel as we elaborated in Section 2.4 and Fig. 4. This is also seen in the measured signals extracted across multiple pixels in the neighborhood of the corresponding spot (Fig. 8(a)-Fig. 8(c)). This is not a fundamental limitation of the sensor but of the current arrayer configuration and the bio-interface, as we discussed in Section 2.4

3.9. System analysis and limit of detection

The translation of surface sensitivity to volume sensitivity for assays is a strong function of the assay chemistry, the diffusion mechanism of the target nucleic acid or protein in the bulk solution (that is influenced by the flow and design of the reaction chamber) [75]. However, the core surface sensitivity of the sensor in its ability to detect the minimum number of fluorescence labels on the surface (after the assay and washing steps) can be analytically derived based on both the optical and electronic performances of the components. This including the filter rejection ratio, sensor responsivity, output noise and integration time. Once the surface sensitivity is determined, volume sensitivity for assays can be optimized through careful design of the flow process and the assay protocol.

Here, we analyze the surface sensitivity of the sensor based on the measurements of the optical and electronic characteristics and compare with the directly measured performance. The fundamental limit of the sensor to surface sensitivity is not only limited by the noise of the detector (contributed primarily by the shot noise, circuit readout noise and the quantization noise after digitization), but also by the standard error of the chemical binding process when the assay is repeated. Consider P_f as the fluorescence light power, R_f as the photodiode responsivity (A/W) at the fluorescence wavelength, T as the integration time and e as the electron charge. Then the signal power after the integration time (expressed as a number of electron charges) is given by

$$P_{sig} = \frac{P_f R_f T}{e} \quad (3)$$

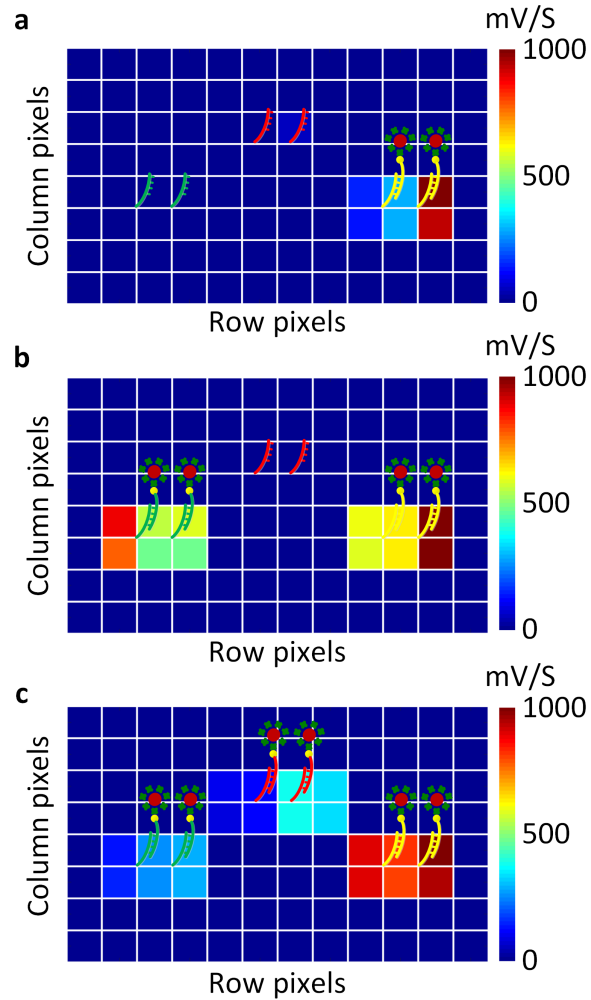


Fig. 8. **a, b, c**, Measured multiplexed detection capability of the sensor array with different DNA capture strands showing positive responses at the conjugated site and almost no signal at the non-specific sites. As the glass slip is $100\ \mu\text{m}$ from the sensor surface, we can see fluorescence emission spreading across multiple pixels (each square is a sensor site). This is not a fundamental limitation of the sensor, but arises as a result of the spacing between the chip and the bio-interface.

Evidently, higher integration time increases the signal power, but it is ultimately limited by the finite rejection ratio of the implemented filter that causes the detector to saturate to the highest allowable voltage swing V_{SW} . The maximum integration time is given by

$$T = T_{max} = \frac{V_{SW} C_{fb}}{(P_f + \frac{P_l}{\beta}) R_f} \quad (4)$$

where P_l is the excitation light power and β is the filter rejection ratio. As can be seen, a stronger filtering ratio allows a higher integration time boosting the signal. Therefore, it is critical to ensure robust filtering performance as demonstrated in the paper, allowing a ratio between 45-60 dB across angles of incidence (Fig. 5).

On the other hand, total standard error at the output is composed of sensing circuits noise, readout noise, photon shot noise, LED power fluctuation, and standard error of the assay or biological noise. This can be collectively expressed as

$$P_n = \sqrt{\left(\frac{V_{Ncir} C_{fb}}{e}\right)^2 + \left(\frac{V_{Nadc} C_{fb}}{e}\right)^2 + \frac{(P_f + \frac{P_l}{\beta}) R_f T}{e} + \left(\frac{\eta_{ex} (P_f + \frac{P_l}{\beta}) R_f T}{e}\right)^2 + \left(\frac{\eta_{bio} P_f R_f T}{e}\right)^2} \quad (5)$$

Here, V_{Ncir} is the photosensing circuits noise, C_{fb} is the feedback capacitance of the CTIA, V_{Nadc} is the readout and quantization noise, η_{ex} represents the normalized standard deviation of the fluctuation of the LED excitation power, and η_{bio} represents the biological noise.

Since the photon shot noise is dominant, and $\sqrt{P_{n,ph}^2} = \sqrt{\frac{(P_f + \frac{P_l}{\beta}) R_f T}{e}} \propto \sqrt{T}$, from (3) and (5) SNR can be seen to increase monotonically with integration time T till it reaches the maximum value in (4). Using this maximum integration time, the minimum detectable fluorescence signal as a fraction of the incident excitation light for a signal-to-noise ratio (SNR) of one can be derived to be

$$\frac{P_l}{P_f} (SNR = 1) = \beta \sqrt{\frac{1 - \eta_{bio}^2}{\eta_{ex}^2 + \frac{V_{Ncir}^2 + V_{Nadc}^2}{V_{SW}^2} + \frac{e}{V_{SW} C_{fb}}}} - 1 \approx \beta \sqrt{\frac{1 - \eta_{bio}^2}{\eta_{ex}^2 + \frac{V_{Ncir}^2 + V_{Nadc}^2}{V_{SW}^2} + \frac{e}{V_{SW} C_{fb}}}} \quad (6)$$

As described in Section 3.3, the measured r.m.s noise voltage is 3.5 mV. This can be expressed as $V_{Total} = \sqrt{(V_{SW} \eta_{ex})^2 + V_{Ncir}^2 + V_{Nadc}^2 + \frac{e V_{SW}}{C_{fb}}}$ and includes the LED fluctuations, circuits and read out noise and photon shot noise. However, with multiple signal acquisition (~ 100 times) for each sensing pixel, the total noise can be further reduced by simple averaging, nearly 7 dB below the measured level to $V_{Total} \approx 0.7$ mV. The reduction is less than 10 dB expected from a white noise process, due to the contribution of the $1/f$ noise of the circuits.

In summary, in our design, we measure the following parameters

- The maximum allowable voltage swing V_{SW} is measured to be around 1 V.
- The rejection ratio (β) varies between 45-60 dB (Fig. 5) and we assume here the worst case value of 45 dB.

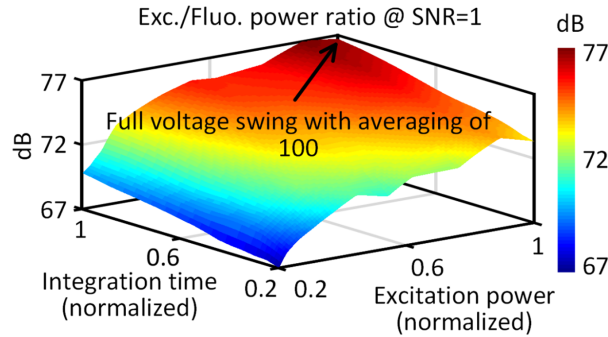


Fig. 9. **a.** Variation of achievable sensitivity expressed as P_{ex}/P_{fl} for a SNR=1 with signal power and integration time. Maximizing the integration time to maximize achievable voltage swing allows this ratio to reach nearly 77 dB. This is achieved with an initial pre-filtering of 45-60 dB optically with the nanoplasmonic filters and the remaining background suppression is achieved electronically.

- The standard error for assay variation *i.e.* the biological noise is estimated to be $\eta_{bio} = 20\%$
- Measured $V_{Total} \approx 0.7$ mV after averaging.

Utilizing these values, the maximum ratio between fluorescence and excitation signal can be estimated to be to be $P_{fl}/P_{ex} \approx -77$ dB for the implemented system. The Qdot800 that we use in this work has the absorption coefficient of $1.06 \times 10^7 \text{ cm}^{-1} \text{ M}^{-1}$ that translates to a molecular absorption cross section of $1.76 \times 10^{-14} \text{ cm}^2$. Assuming the estimated quantum efficiency of 0.5, $P_{fl}/P_{ex} \approx -77$ dB translates to a detection limit of $0.23 \text{ dot}/\mu\text{m}^2$ with a SNR=1. For a SNR of 3-4, the theoretical limit corresponds to $0.7\text{-}1 \text{ dot}/\mu\text{m}^2$ which is very close to the measured value as shown in Fig. 7(a).

The electronic-photonics co-design approach allows us to reach levels of $P_{fl}/P_{ex} \approx -77$ dB through a combination of optical and electronic filtering and processing across multiple stages. A initial pre-filtering of 45-60 dB is achieved optically with the nanoplasmonic filters. The remaining suppression of the background is enabled electronically with a control site, and noise minimization by multiple acquisition and averaging (100 acquisitions in less than 1 minute). The sensor design itself uses interlaid differential sensing (Fig. 3) to minimize the effect of dark currents. The achievable sensitivity varies with both signal power and integration time as captured in Fig. 9. This co-design and integration methodology allows us to collectively reach towards sensitivity levels approaching that of commercial ELISA platforms.

4. Conclusion and discussion

In conclusion, we present for the first time external optics-free nano-optical fluorescence 96-sensor-array in CMOS with sensitivities of commercial ELISA readers. The salient features of the system can be summarized as below

- We demonstrate for the first time integration of complex nanoplasmonic structures and active devices in a ‘no change’ approach to an industry-standard CMOS process. This is the key toward such extreme miniaturization and it enables a new class of angle-insensitive nanoplasmonic filtering (45-60 dB) across a massively parallelized chip-scale platform. This filtering characteristic is distinct from classical interference-based or plasmonics-based resonant structures allowing us to eliminate all external optics and miniaturize the entire system to such an extent.

- The work demonstrates the strength of electronic/nano-optic co-integration, co-design and cross-layer optimization, where 45-50 dB of filtering is achieved optically, and 25-30 dB of subsequent electronic filtering allowing us to reach fluorescence detection limits of nearly 77 dB below the excitation signal.
- The system demonstrates measured detection limits down to zeptomoles of fluorophores on the surface ($\sim 1 \text{ dot}/\mu\text{m}^2$ of surface density) and $\sim 100 \text{ fM}$ and $\sim 5 \text{ pM}$ respectively, comparable to commercial fluorescence-based readers and ELISA-based detection systems. Further, being realized in a fully integrated CMOS process with no post-processing, this can enable future point-of-care systems at extremely low-cost by incorporating the sensing interface, sensing platform and the reader all integrated into the chip.
- In addition, the entire nano-optical system including the source, occupies less than 0.1 cc in volume potentially enabling future in-vivo bimolecular sensing modalities.

The ability of a CMOS system to detect fluorescence quantum-dots down to zeptomole level ($\sim 1 \text{ dot}/\mu\text{m}^2$ of surface density) is a promising sign where more complex multi-modal sensing systems can be envisioned for future sensing applications. While the system sensitivities of $\sim 100 \text{ fM}$ and $\sim 5 \text{ pM}$ respectively are lower than other works utilizing plasmonic enhancement [48], gold nanoparticle labels [71], fibre-optic readouts [72, 73], organometallic labels [74] and GMR sensors [75], it is comparable to commercial fluorescence based readers and ELISA-based detection and reader systems and therefore suitable for a wide range of molecular diagnostic applications in clinical and research settings.

Currently, sensitivity is partly limited by the poor quantum efficiency of the diodes (Q.E. ~ 0.1) in the implemented process and can be further increased by migrating to a CMOS-based imager process with similar feature size. We are also investigating the light delivery mechanism for a more uniform illumination. While the variation is not large enough to cause Qdot photo-bleaching and can be addressed with an automated calibration process, it is still important to enhance the uniformity as much as possible. Uniformity of background can ensure similar dynamic range across all the sensor pixels. This requires modification of the light delivery mechanism. While we currently allow the LED to shine directly on the chip, pixel-to-pixel variation in the background can be reduced by coupling light through an optical fiber and employing a diffuser above the chip. Co-design of the electronic and optical packaging is critical to the sensor performance, and we are currently investigating methods to allow a more uniform illumination.

When compared to commercially available biochip such as Affimetrix, it can be noted that the presented sensor array does not need an additional reader. It encompasses the sensor platform, sensors and reader all integrated into the chip (with the source being closely packaged as well). Quantum dot based assays have matured over the years, and we employ these labels to allow the scattering and angle insensitive filtering. This is the key to miniaturization, where the light path is not collimated unlike bulky fluorescence readers.

While a 96-sensor array is demonstrated in this paper, given the integration capability of both electronics and future nano-optics, the technology can be potentially scaled into tens of thousands, if not hundreds of thousands of sensing sites, in a scalable and cost-effective manner. Of course, the entire system is more than the sensor. Scaling of CMOS-based bio-sensing platforms including packaging and functionalization is expectedly a multi-step process that is likely to be handled by different facilities. While this can involve varying degrees of cost, it is in line with manufacturing of commercial electronic systems where chip fabrication, packaging, assembly and testing are carried out in different facilities. Typically, the costs are split evenly across these different steps. Similar partition of the manufacturing cost can be envisioned for CMOS-based biosensing systems. Both IC fabrication and bio-functionalization are standardized processes and can be carried out separately, and a final packaging step can bring these parts together for a complete system. This does not negate the significant cost reduction in the entire

system, since it eliminates the complexity and cost of the reader system. More importantly through miniaturization and possible integration of a wireless interface in the sensor, it can enable a new eco-system of connected biosensors deployable at point of care.

With the ability to interface with digital microfluidics in future [77, 78], this can enable new complex ultra-miniaturized sample-to-answer biomedical devices that have the great potential to be deployed at the point-of-care for both in-vitro and in-vivo applications.

Funding

National Science Foundation (NSF) (1610761,1711067), Qualcomm Innovation Fellowship, Princeton Project X, Princeton Intellectual Property Fund.

Acknowledgments

We would like to thank all the members of the Sengupta Lab and Yang Lab for technical discussions.

Disclosures

The authors declare that there are no conflicts of interest related to this article.

References and links

1. W. Xu, K.M. Chan, and E.T. Kool, "Fluorescent nucleobases as tools for studying DNA and RNA," *Nat. Chem.* **9**, 1043–1055 (2017).
2. Z. Pode, R. Peri-Naor, J.M. Georgeson, T. Ilani, V. Kiss, T. Unger, B. Markus, H.M. Barr, L. Motiei, and D. Margulies, "Protein recognition by a pattern-generating fluorescent molecular probe," *Nat. Nanotech.* **12**, 1161–1168 (2017).
3. Y. Long, Y. Stahl, S. Weidtkamp-Peters, M. Postma, W. Zhou, J. Goedhart, M. Sanchez-Perez, T. Gadella, R. Simon, B. Scheres, and I. Blilou, "In vivo FRET-FLIM reveals cell-type-specific protein interactions in Arabidopsis root," *Nature* **548**, 97–102 (2017).
4. J.R. Heath, A. Ribas, and P.S. Mischel, "Single-cell analysis tools for drug discovery and development," *Nat. Reviews Drug Discovery* **15**, 204–216 (2016).
5. H. Choi, J.Y. Chang, L.A. Trinh, J.E. Padilla, S.E. Fraser, and N.A. Pierce, "Programmable in situ amplification for multiplexed imaging of mRNA expression," *Nat. Biotech.* **28**, 1208–1212 (2010).
6. K. Si, R. Fiolka, and M. Cui, "Fluorescence imaging beyond the ballistic regime by ultrasound-pulse-guided digital phase conjugation," *Nat. Photon.* **6**, 657–661 (2012).
7. Y.M. Wang, B. Judkewitz, C.A. DiMarzio, and C. Yang, "Deep-tissue focal fluorescence imaging with digitally time-reversed ultrasound-encoded light," *Nat. Comm.* **3**, 928 (2012).
8. L. Camborde, A. Jauneau, C. Briere, L. Deslandes, B. Dumas, and E. Gaulin, "Detection of nucleic acid-protein interactions in plant leaves using fluorescence lifetime imaging microscopy," *Nat. Protocols* **12**, 1933–1950 (2017).
9. J. Querard, R. Zhang, Z. Kelemen, M. Plamont, X. Xie, R. Chouket, I. Roemgens, Y. Korepina, S. Albright, E. Ipendey, M. Volovitch, H. L. Sladitschek, P. Neveu, L. Gissot, A. Gautier, J. Faure, V. Croquette, T.L. Saux, and L. Jullien, "Resonant out-of-phase fluorescence microscopy and remote imaging overcome spectral limitations," *Nat. Comm.* **8**, 969 (2017).
10. A.P. Alivisatos, A.M. Andrews, E.S. Boyden, M. Chun, G.M. Church, K. Deisseroth, and S. Masmanidis, "Nanotools for neuroscience and brain activity mapping," *ACS Nano*, **7**, 1850–1866 (2013).
11. M. Monge, A. Lee-Gosselin, M.G. Shapiro, and A. Emami, "Localization of microscale devices in vivo using addressable transmitters operated as magnetic spins," *Nat. Biomed. Eng.* **1**, 736–744 (2017).
12. M. Sitti, H. Ceylan, W. Hu, J. Giltinan, M. Turan, S. Yim, and E. Diller, "Biomedical applications of untethered mobile milli/microrobots," *Proc. IEEE* **103**, 205–224 (2015).
13. L. Liu, S. Towfighian, and A. Hila, "A review of locomotion systems for capsule endoscopy," *IEEE Rev. Biomed. Eng.* **8**, 138–151 (2015).
14. G. Ciuti, A. Menciassi, and P. Dario, "Capsule endoscopy: from current achievements to open challenges," *IEEE Rev. Biomed. Eng.* **4**, 59–72 (2011).
15. D. Seo, R.M. Neely, K. Shen, U. Singhal, E. Alon, J.M. Rabaey, and M.M. Maharbiz, "Wireless recording in the peripheral nervous system with ultrasonic neural dust," *Neuron*, **91**, 529–539 (2016).
16. B.J. Williams, S.V. Anand, J. Rajagopalan and M.T. Saif, "A self-propelled biohybrid swimmer at low Reynolds number," *Nat. Commun.*, **5**, 3081 (2014).
17. B.J. Nelson, I.K. Kaliaatsos, and J.J. Abbott, "Microrobots for minimally invasive medicine," *Annu. Rev. Biomed. Eng.*, **12**, 55–85 (2010).

18. J. Breault-Turcot, H.P. Poirier-Richard, M. Couture, D. Pelechacz, and J.F. Masson, "Single chip SPR and fluorescent ELISA assay of prostate specific antigen," *Lab Chip* **15**, 4433–4440 (2015).
19. L. Sandeau, C. Vuillaume, S. Contie, E. Grinval, F. Belloni, H. Rigneault, and M.B. Fournet, "Large area CMOS bio-pixel array for compact high sensitive multiplex biosensing," *Lab Chip* **15**, 877 (2015).
20. K.K. Ghosh, L.D. Burns, E.D. Cocker, A. Nimmerjahn, Y. Ziv, A. El Gamal, and M.J. Schnitzer, "Miniaturized integration of a fluorescence microscope," *Nat. Meth.* **8**, 871–878 (2011).
21. M. Kuhnemund, Q. Wei, E. Darai, Y. Wang, I. Hernández-Neuta, Z. Yang, and A. Ozcan, "Targeted DNA sequencing and in situ mutation analysis using mobile phone microscopy," *Nat. Comm.* **8**, 13913 (2017).
22. M.A. Al-Rawhani, J. Beeley, and D.R. Cumming, "Wireless fluorescence capsule for endoscopy using single photon-based detection," *Sci. Rep.* **5**, 18591 (2015).
23. G. Xu, J. Abbott, L. Qin, K.Y. Yeung, Y. Song, H. Yoon, and D. Ham, "Electrophoretic and field-effect graphene for all-electrical DNA array technology," *Nat. Comm.* **5**, 4866 (2014).
24. C.W. Huang, Y.J. Huang, P.W. Yen, H.H. Tsai, H.H. Liao, Y.Z. Juang and C.T. Lin, "A CMOS wireless biomolecular sensing system-on-chip based on polysilicon nanowire technology," *Lab on a Chip* **13**, 4451–4459 (2013).
25. P.B. Stranges, M. Palla, S. Kalachikov, J. Nivala, M. Dorwart, S. Kumar, and Z. Li, "Design and characterization of a nanopore-coupled polymerase for single-molecule DNA sequencing by synthesis on an electrode array," *PNAS* **113**, E6749–E6756 (2016).
26. H. Norian, R.M. Field, I. Kymissis, and K.L. Shepard, "An integrated CMOS quantitative-polymerase-chain-reaction lab-on-chip for point-of-care diagnostics," *Lab on a Chip*, **14**, 4076–4084 (2014).
27. D. Ha, J. Paulsen, N. Sun, Y.Q. Song and D. Ham, "Scalable NMR spectroscopy with semiconductor chips," *PNAS* **111**, 11955–11960 (2014).
28. Y. Huang, and A.J. Mason, "Lab-on-CMOS integration of microfluidics and electrochemical sensors," *Lab on a Chip*, **13**, 3929–3934 (2013).
29. D.L. Bellin, H. Sakhtah, Y. Zhang, A. Price-Whelan, L.E. Dietrich, and K.L. Shepard, "Electrochemical camera chip for simultaneous imaging of multiple metabolites in biofilms," *Nat. Comm.* **7**, 10535 (2016).
30. J. Abbott, T. Ye, L. Qin, M. Jorgolli, R.S. Gertner, D. Ham, and H. Park, "CMOS nanoelectrode array for all-electrical intracellular electrophysiological imaging," *Nat. Nanotech.* **12**, 460–466 (2017).
31. D. Tsai, D. Sawyer, A. Bradd, R. Yuste, and K.L. Shepard, "A very large-scale microelectrode array for cellular-resolution electrophysiology," *Nat. Comm.* **8**, 1802 (2017).
32. J. Müller, M. Ballini, P. Livi, Y. Chen, M. Radivojevic, A. Shadmani and A. Stettler, "High-resolution CMOS MEA platform to study neurons at subcellular, cellular, and network levels," *Lab on a Chip* **15**, 2767–2780 (2015).
33. A. Pai, A. Khachaturian, S. Chapman, A. Hu, H. Wang, and A. Hajimiri, "A handheld magnetic sensing platform for antigen and nucleic acid detection," *Analyst* **139**, 1403–1411 (2014).
34. H. Wang, A. Mahdavi, D.A. Tirrell, and A. Hajimiri, "A magnetic cell-based sensor," *Lab on a Chip* **12**, 4465–4471 (2012).
35. A. Manickam, R. Singh, M.W. McDermott, N. Wood, S. Bolouki, P. Naraghi-Arani, and A. Hassibi, "A Fully Integrated CMOS Fluorescence Biochip for DNA and RNA Testing," *IEEE J. Solid-State Circuits* **52**, 2857–2870 (2017).
36. B. Jang, P. Cao, A. Chevalier, A. Ellington, and A. Hassibi, "A CMOS fluorescent-based biosensor microarray," *IEEE Intl. Solid-State Circuits Conf.* 436–437 (2009).
37. D. Ho, M.O. Noor, U.J. Krull, G. Gulak, and R. Genov, "CMOS Spectrally-Multiplexed FRET-on-a-Chip for DNA Analysis," *IEEE Trans. Biomedical Circuits and Sys.* **7**, 643–654 (2013).
38. M.W. Seo, K. Kagawa, K. Yasutomi, Y. Kawata, N. Teranishi, Z. Li, and S. Kawahito, "A 10 ps Time-Resolution CMOS Image Sensor With Two-Tap True-CDS Lock-In Pixels for Fluorescence Lifetime Imaging," *IEEE J. Solid-State Circuits* **51**, 141–154 (2016).
39. R.M. Field, S. Realov, and K.L. Shepard, "A 100 fps, Time-Correlated Single-Photon-Counting-Based Fluorescence-Lifetime Imager in 130 nm CMOS," *IEEE J. Solid-State Circuits* **49**, 867–880 (2014).
40. D.K. Gramotnev, and S.I. Bozhevolnyi, "Plasmonics beyond the diffraction limit," *Nat. Photon.* **4**, 83–91 (2010).
41. J.B. Khurgin, "How to deal with the loss in plasmonics and metamaterials," *Nat. Nanotech.* **10**, 2–6 (2015).
42. J.A. Schuller, "Plasmonics for extreme light concentration and manipulation," *Nat. Mat.* **9**, 193–204 (2010).
43. S. Kawata, Y. Inouye, and P. Verma, "Plasmonics for near-field nano-imaging and superlensing," *Nat. Photon.* **3**, 388–394 (2009).
44. H.W. Lee, G. Papadakis, S.P. Burgos, K. Chander, A. Kriesch, R. Pala, and H.A. Atwater, "Nanoscale Conducting Oxide PlasMOStor," *Nano Lett.* **14**, 6463–6468 (2014).
45. N. Meinzer, W.L. Barnes, and I.A. Hooper, "Plasmonic meta-atoms and metasurfaces," *Nat. Photon.* **8**, 889–898 (2014).
46. N. Yu and F. Capasso, "Flat optics with designer metasurfaces," *Nat. Mat.* **13**, 139–150 (2014).
47. A.G. Brolo, "Plasmonics for future biosensors," *Nat. Photon.* **6**, 709–713 (2012).
48. L. Zhou, F. Ding, H. Chen, W. Ding, W. Zhang, and S.Y. Chou, "Enhancement of Immunoassay's Fluorescence and Detection Sensitivity Using Three-Dimensional Plasmonic Nano-Antenna-Dots Array," *Anal. Chem.* **84**, 4489–4495 (2012).
49. A. Fratolocci, C.M. Dodson, R. Zia, P. Genevet, E. Verhagen, H. Altug, and V.J. Sorger, "Nano-optics gets practical," *Nature Nanotech.* **10**, 11–15 (2015).

50. D.Y. Fedyanin, D.I. Yakubovsky, R.V. Kirtaev, and V.S. Volkov, "Ultralow-Loss CMOS Copper Plasmonic Waveguides," *Nano Lett.*, **16**, 362–366 (2015).
51. L. Hong, H. Li, H. Yang, and K. Sengupta, "Fully integrated fluorescence biosensors on-chip employing multi-functional nanoplasmonic optical structures in CMOS," *IEEE J. Solid-State Circuits* **52**, 2388 (2017).
52. D.D. TDalma-Weiszhausz, J. Warrington, E.Y. Tanimoto, and C.G. Miyada, "The Affymetrix GeneChips platform: an overview," *Methods Enzymol.* **410**, 3–28 (2006).
53. L. Shi, L.H. Reid, W.D. Jones, R. Shippy, J.A. Warrington, S.C. Baker, and Y. Luo, "The MicroArray Quality Control (MAQC) project shows inter- and intraplatform reproducibility of gene expression measurements," *Nat. Biotechnol.* **24**, 1151–1161 (2006).
54. N. Scholler, M. Crawford, A. Sato, C.W. Drescher, K.C. O'Brian, N. Kiviat, and N. Urban, "Bead-based ELISA for validation of ovarian cancer early detection markers," *Clin. Cancer Res.* **12**, 2117–2124 (2006).
55. D.M. Shcherbakova and V.V. Verkhusha, "Near-infrared fluorescent proteins for multicolor in vivo imaging," *Nat. Methods* **10**, 751–754 (2013).
56. X. Michalet, F.F. Pinaud, L.A. Bentolila, J.M. Tsay, S. Doose, J.J. Li, and S. Weiss, "Quantum Dots for Live Cells, in Vivo Imaging, and Diagnostics," *Science* **307**, 538–544 (2005).
57. R. Atreya, H. Neumann, C. Neufert, M.J. Waldner, U. Billmeier, Y. Zopf, and S. Maas, "In vivo imaging using fluorescent antibodies to tumor necrosis factor predicts therapeutic response in Crohn's disease," *Nat. Med.* **20**, 313–318 (2014).
58. W. Lukosz and R.E. Kunz, "Light emission by magnetic and electric dipoles close to a plane interface. I. Total radiated power," *JOSA* **67**, 1607–1615 (1977).
59. W. Lukosz and R.E. Kunz, "Light emission by magnetic and electric dipoles close to a plane dielectric interface. II. Radiation patterns of perpendicular oriented dipoles," *JOSA* **67**, 1615–1619 (1977).
60. W. Lukosz, "Light emission by magnetic and electric dipoles close to a plane dielectric interface. III. Radiation patterns of dipoles with arbitrary orientation," *JOSA* **69**, 1495–1503 (1979).
61. T. Xu, Y. Wu, X. Luo, and L.J. Guo, "Plasmonic nanoresonators for high-resolution colour filtering and spectral imaging," *Nat. Comm.* **1**, 59 (2010).
62. S. Yokogawa, S. P. Burgos, and H. Atawater, "Plasmonic Color Filters for CMOS Image Sensor Applications," *Nano Lett.* **12**, 4349–4354 (2012).
63. S. Jayasuriya, S. Sivaramakrishnan, E. Chuang, D. Gururibam, A. Wang, and A. Molnar, "Dual light field and polarization imaging using CMOS diffractive image sensors," *Optics Letters* **40**, 2433–2436 (2015).
64. L. Hong, H. Li, H. Yang, and K. Sengupta, "Integrated Angle-insensitive Nano-plasmonic Filters for Ultraminiaturized Fluorescence Microarray in a 65-nm Digital CMOS Process," *ACS Photonics*, accepted [10.1021/acsp Photonics.8b00440] (2018).
65. L. Hong and K. Sengupta, "Fully Integrated Optical Spectrometer in Visible and Near-IR in CMOS," *IEEE Trans. Biomedical Circuits and Systems* **11**, 1176–1191 (2017).
66. X. Lu, L. Hong and K. Sengupta, "CMOS Optical PUFs Using Noise-Immune Process-Sensitive Photonic Crystals Incorporating Passive Variations for Robustness," *IEEE J. Solid-State Circuits* **53**, 2709–2721 (2018).
67. L. Hong and K. Sengupta, "Fully integrated optical spectrometer with 500-to-830nm range in 65nm CMOS," in *IEEE Intl. Solid-State Circuits Conference (ISSCC)* (2017), pp. 462–463.
68. X. Lu, L. Hong and K. Sengupta, "15.9 An integrated optical physically unclonable function using process-sensitive sub-wavelength photonic crystals in 65nm CMOS," in *IEEE Intl. Solid-State Circuits Conference (ISSCC)* (2017), pp. 272–273.
69. L. Hong, X. Lu and K. Sengupta, "Nano-optical systems in CMOS," in *IEEE Intl. Midwest Symp. Circuits and Systems (MWSCAS)* (2017), pp. 906–909.
70. ThermoFisher Scientific, Qdot 800 Streptavidin Conjugate. <https://www.thermofisher.com/order/catalog/product/Q10171MP>. Accessed February 07, 2018.
71. X. Yao, X. Li, F. Toledo, C. Zurita-Lopez, M. Gutova, J. Momand, and F. Zhou, "Sub-attomole oligonucleotide and p53 cDNA determinations via a high-resolution surface plasmon resonance combined with oligonucleotide-capped gold nanoparticle signal amplification," *Anal. Biochem.* **354**, 220–228 (2006).
72. L. Song, S. Ahn, and D.R. Walt, "Fiber-optic microsphere-based arrays for multiplexed biological warfare agent detection," *Anal. Chem.* **78**, 1023–1033 (2006).
73. M. Bowden, L. Song, and D.R. Walt, "Development of a microfluidic platform with an optical imaging microarray capable of attomolar target DNA detection," *Anal. Chem.* **77**, 5583–5588 (2005).
74. H. Xie, C. Zhang, and Z. Gao, "Amperometric detection of nucleic acid at femtomolar levels with a nucleic acid/electrochemical activator bilayer on gold electrode," *Anal. Chem.* **76**, 1611–1617 (2004).
75. R.S. Gaster, L. Xu, S.J. Han, R.J. Wilson, D.A. Hall, S.J. Osterfeld, and S.X. Wang, "Quantification of protein interactions and solution transport using high-density GMR sensor arrays," *Nat. Nanotech.* **6**, 314–320 (2011).
76. U. Resch-Genger, M. Grabolle, S. Cavaliere-Jaricot, R. Nitschke, and T. Nann, "Quantum dots versus organic dyes as fluorescent labels," *Nat. Methods* **5**, 763–775 (2008).
77. T. Datta-Chaudhuri, P. Abshire, and E. Smela, "Packaging commercial CMOS chips for lab on a chip integration," *Lab on a Chip* **14**, 1753–1766 (2014).
78. D.H. Kuan, I.S. Wang, J.R. Lin, C.H. Yang, C.H. Huang, Y.H. Lin, and N.T. Huang, "A microfluidic device integrating dual CMOS polysilicon nanowire sensors for on-chip whole blood processing and simultaneous detection of multiple

analytes,” *Lab on a Chip* **16**, 3105–3113 (2016).